URTeC Control ID Number: 1619856

Distance Metric Based Multi-Attribute Seismic Facies Classification to Identify Sweet Spots within the Barnett shale: A Case Study from the Fort Worth Basin, TX

Atish Roy, University of Oklahoma
Vikram Jayaram, Oklahoma Geological Survey
Kurt Marfurt, University of Oklahoma

This paper was prepared for presentation at the Unconventional Resources Technology Conference held in Denver, Colorado, USA, 12-14 August 2013.

Summary

Conventional reservoirs benefit from a long scientific history that correlates successful plays to seismic measurements through depositional, tectonic, and digenetic models. Unconventional reservoirs are less well understood, however benefit from significantly denser well control. Thus, allowing us to establish statistical rather than model-based correlations between seismic data, geology, and successful completion strategies. One of the more commonly encountered correlation techniques is based on computer assisted pattern recognition. The pattern recognition techniques have found their niche in a plethora of applications ranging from flagging suspicious credit card purchase patterns to rewarding repeating online buying patterns. Classification of a given seismic response as having a “good” or “bad” pattern requires a “distance metric”. Distance metric “learning” uses past experiences (well performance) as training data to develop a distance metric. Alternative distance metrics have demonstrated significant value in the identification and classification of repeated or anomalous behaviors in public health, security, and marketing. In this paper we examine the value of three of these alternative distance metrics of 3D seismic attributes to the identification of sweet spots in a Barnett Shale play.

Introduction

Similarity of waveforms or attribute patterns along a horizon to those about good and bad wells is a well-established practice in seismic data interpretation. In such studies, typically, the interpreter compares a vector of samples (e.g. Johnson, 2000) or attributes (e.g. Michelena et al., 1998) extracted from productive or non-productive wells to every trace along the horizon**.** Poupon et al. (1999) correlated wells to seismic waveforms, where the supervision was not only the actual seismic about the well but also a suite of synthetic seismic traces generated through petrophysical modeling and fluid substitution. The performance of these algorithms can depend delicately on the manner in which distances are measured. Distance metrics are a vital component in many applications ranging from supervised learning and clustering to product recommendations and document browsing. Since, designing such metrics by hand is difficult, we look at the problem of learning a metric from exemplars. In particular, we consider relative and qualitative exemplars of the form “**P** is closer to **Q** than **P** is to **R**”. In essence, a distance metric is a mathematical operator that conveys how similar two (possibly vector-valued) members of a set compared with a single, scalar value, based on a notion of similarity. The most common and most easily understood waveform similarity metric is based on Euclidian distance.

In this paper, we discuss three different schemes of distance measures to classify 3D seismic facies: the minimum Euclidean distance (MED), spectral angle mapper (SAM) and the Bhattacharya distance, to quantify similarity to a given suite of wells. The use of such well control makes this a “supervised” learning task, with each seismic voxel being clustered with the most similar well. Depending on our distance scalar, we may choose to leave some voxels as “unclassified”.

We begin our analysis by providing brief formulations of the three distance metric methods utilized in the paper. We then summarize the training step and the generation of seismic facies volumes. Lastly, we discuss how each distance metric uniquely identifies and maps facies for sweet spot detection within the Barnett shale.

Minimum Euclidean Distance

Throughout this paper we have compared two types of vectors. One is the attribute data-vector $\mathbf{P}_n$, which are the normalized attribute values at each voxel location n. The other is the well data-vector $\mathbf{Q}_w$, which is the average of the attribute data-vector around each well location w. In a Cartesian coordinate system, the Euclidean distance between vectors $\mathbf{P}_n$ and $\mathbf{Q}_w$ is described as the length of the distance connecting the two vectors. This distance metric is valid and can be extended to an N-dimensional space, where n is the number of seismic attributes at any voxel. The formulation of the distance between $\mathbf{P}_n$ and $\mathbf{Q}_w$ for a single well location w is given by

$$d_{Euclidian}(\mathbf{P}, \mathbf{Q}_w) = \sqrt{\sum_{j=1}^{N} |\mathbf{P}_n - \mathbf{Q}_w|^2}, \ldots\ldots\ldots\ldots\ldots\ldots\ldots\ldots (1)$$

where, $\mathbf{P}_n$ is the vector at n^{th} voxel and $\mathbf{Q}_w$ is the vector at w^{th} well.

Also, to be noted that the distances such as the Euclidean distance, have some well-known properties such as

- $d(\mathbf{P}, \mathbf{Q}) \geq 0$ for all p and q and $d(\mathbf{P}, \mathbf{Q}) = 0$ only if $\mathbf{P}=\mathbf{Q}$ (Positive definiteness)
- $d(\mathbf{P}, \mathbf{Q}) = d(\mathbf{Q}, \mathbf{P})$ for all p and q (Symmetry)
- $d(\mathbf{P}, \mathbf{R}) \leq d(\mathbf{P}, \mathbf{Q}) + d(\mathbf{Q}, \mathbf{R})$ for all points $\mathbf{P}$, $\mathbf{Q}$, and $\mathbf{R}$ (Triangle Inequality),

where, $d(\mathbf{P}, \mathbf{Q})$ is the distance (dissimilarity) between points (data objects), $\mathbf{P}$ and $\mathbf{Q}$ are vectors. A distance that satisfies these properties is a metric, and such a space is called a metric space.

The Euclidean distance is a special case of *Mahalanobis* distance measure, which is formulated as $d_{Mahalanobis}(\mathbf{P},\mathbf{Q}) = (\mathbf{P}-\mathbf{Q})\sum^{-1}(\mathbf{P}-\mathbf{Q})^T$. When the covariance matrix, $\mathbf{\Sigma}$, is identity matrix, the *Mahalanobis* distance is the same as the Euclidean distance.

Spectral Angle Mapper

The mathematical formulation of SAM attempts to obtain the angles formed between the reference well data-vector $\mathbf{Q}_w$, and the attribute data-vector $\mathbf{P}_n$, treating them as vectors in a space with dimensionality equal to the number of attributes (Kruse et al., 1992; Boardman, 1992). SAM presents the following formulation:

$$\alpha = \cos^{-1} \frac{\sum \mathbf{P}.\mathbf{Q}}{\sqrt{\sum(\mathbf{P})^2}.\sqrt{\sum(\mathbf{Q})^2}} \ldots\ldots\ldots\ldots\ldots\ldots\ldots\ldots (2)$$

where, α is the angle formed between the well data vector and the attribute data vector. The expression is simply the dot product of vectors $\mathbf{P}$ and $\mathbf{Q}$. The SAM value is expressed in degrees where α is the angle subtended by the two vectors $\mathbf{P}$ and $\mathbf{Q}$, higher the angle means better the separation between the two vectors. The angle α, determined by $\cos^{-1}$, presents a variation anywhere between 0 degree and 90 degree. Equation 2 can also be expressed as

$$\cos\alpha = \frac{\sum \mathbf{P}.\mathbf{Q}}{\sqrt{\sum(\mathbf{P})^2}.\sqrt{\sum(\mathbf{Q})^2}}, \ldots\ldots\ldots\ldots\ldots\ldots\ldots\ldots (3)$$

where, the best estimate acquires values close to 1.

The Bhattacharya Distance

In this metric, we use a probability distribution functions to measure similarities or dissimilarities between two PDFs. Initially we define a 2D latent space grid with uniformly defined control points K and we project the posterior probabilities of the vectors onto the grid points $k=1,2,....,K$. Let R_{wk} be the posterior probability distribution corresponding to the w^{th} well data-vector $\mathbf{Q}_w$, at k^{th} grid location of the latent space (Figure 1a). Let R_{nk} be the posterior probability projected at k^{th} grid point, of any n^{th} voxel seismic attribute data-vector $\mathbf{P}_n$ (Figure 1b). Thus each vector $\mathbf{Q}_w$ and $\mathbf{P}_n$ forms a PDF in the defined 2D latent space. Then by Bhattacharya (1943) measure, we can find the similarities (Figure 1c) between the two PDFs by

$$d_n = \sum_{k=1}^{K} \sqrt{R_{wk} R_{nk}} \quad \text{……………………. (4)}$$

where, k are the grid points of the 2D latent space. Thus when two distributions are identical ($R_{nk} = R_{wk}$), we have a coefficient of $d_n = \sum_{k=1}^{K} R_{wk} = 1$. In contrast when there is no overlap between the PDFs $d_n = 0$. Thus, this coefficient ranges from$0 \leq d_n \leq 1$.

For generating the PDF similarity seismic volumes we follow the workflow proposed by Roy (2013) who uses Generative Topographic Mapping (GTM) (Bishop, 1998) to generate a probability density functions (PDFs) of the well vectors and the attribute data-vectors. The GTM is a non-linear dimensional reduction technique that provides a probabilistic representation of the data-vectors in a corresponding lower dimensional latent space.

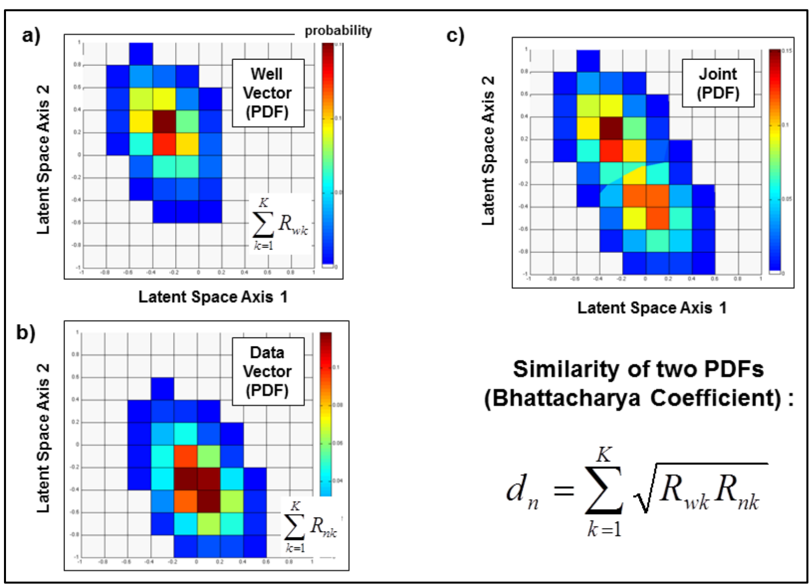

Figure 1: A schematic representation of the supervised GTM analysis workflow: (a) The posterior probability of the well data vector (PDF) projected onto the latent space. (b) The PDF of a data vector corresponding to voxel n in the seismic attribute volume projected onto the latent space. (c) The joint PDF of the average well data vector and the attribute data vector. The coefficient d_n from the Bhattacharya measure is the measure of the similarity (overlap) between the two PDFs.

A set of non-linear continuous and differentiable basis functions is used to map points in the L-dimensional latent space into a lower dimensional non-Euclidean manifold **S** embedded within the D-dimensional data-space. Data vectors are modeled by a suite of Gaussian PDFs centered on the mapped grid points onto the non-Euclidean manifold **S**. This manifold defines the space in which the data vector lies. Each mapped grid point on this 2D manifold holds a finite probability that they represent a data-vector. For the purpose of visualization these probabilities are projected as posterior probabilities back onto the 2D grid space, using Bayes theorem. Initially each target well data-vector forms a PDF in the 2D latent space (Figure 1a). These PDFs are compared with the PDFs of the data-vectors (Figure 1b). In this manner, we compute the overlap value of d_n for all the data-vectors in the survey

(Figure 1c) resulting in a supervised facies "similarity" volume, quantitatively comparing each voxel to good and poor wells (Roy, 2013). Thus, we calculate the overlap of the posterior probability distribution of each of these well data-vectors and the remaining data-vectors by calculating the coefficient from the Bhattacharya (1943) measure (equation 1). Separate "similarity" volumes for each shale petrotype are generated.

Barnett Shale from the Fort Worth Basin

The Fort Worth Basin is a foreland basin, located in north-central Texas and is associated with the late Paleozoic Ouachita orogeny. This basin is bounded by the Muenster Arch to the northeast, the Ouachita Thrust Front to the east, the Bend Arch to the west, the Red River Arch to the north, and the Llano Uplift to the south (Figure 2a). In this study area the Barnett sits on an angular unconformity above the Cambrian to upper-Ordovician-age carbonates of the Ellenberger Group and Viola Formation and overlying Pennsylvanian-age Marble Falls Limestone (Figure 2b). In between, the Forestburg Limestone divides the Barnett formation into Upper and Lower Barnett zone (Figure 2c). The Barnett Shale is not homogeneous, but rather can be subdivided into siliceous shale, argillaceous shale, calcareous shale, and limestone layers, with minor amounts of dolomite (Singh, 2008).

The Fort Worth Barnett shale gas play is traditionally more of an engineering driven play. It requires hydraulic fracturing for gas production. Our 3D seismic survey (Figure 3a) consists of a 200 square mile survey in the North East Fort Worth Basin. The data are sampled at 110ft by 110ft by 2ms. However, the above survey was acquired after numerous vertical and horizontal wells have been drilled and hydraulically fractured. For effective well placement within the survey in future drilling, care should be taken to identify the brittle zones by mapping the geomechanical rock type of the Barnett shale. The dataset between the Marble Faults (overlaying the Barnett formation) and the Viola limestone (below the Barnett formation) are considered for attribute analysis.

Input Seismic Attributes for Seismic Facies classification

The inputs to our algorithms are different seismic inversion volumes (P-impedance, lambda-rho, mu-rho), which help in understanding the highly heterogeneous nature of the Barnett shale. For the above attribute generations the seismic data between the Marble faults horizon and the Viola limestone is considered. The impedance volumes better reflect a heterogeneous shale reservoir based rock type. The Lamé parameters of seismic inversion such as lambda-rho ($\lambda\rho$) and mu-rho ($\mu\rho$) correlate to "fracability" and different elastic properties of rocks. Simple cross-plot between two such elastic properties from the wells sometimes helps in segregating different rock types. However, it is very difficult to separate between classes when we cross-plot any of these two seismic volumes.

We pre-condition our input data so that all the three input attributes are associated with each of the x, y, z location of the survey (we call them as attribute data-vectors). Also the dataset is normalized to remove any bias to one of the input attributes.

Study of the different Petrotypes in Barnett shale

The petrotype analysis for Barnett Shale is done for three different zones with their boundaries defined by the sequences in the gamma-ray log from Figure 3. The Barnett shale is not homogeneous and based on the parasequences, several lithofacies have been defined within the Barnett shale formation (Singh et al, 2008). Analyzing various well logs from the survey, we have considered only three different lithofacies or shale petrotypes : shale petrotype A represents the Upper Barnett Shale, shale petrotype B represents the brittle upper section of Lower Barnett shale, and shale petrotype C represents the ductile, TOC rich lower section of Lower Barnett shale. Zone A is defined within the upper Barnett shale shown in Figure 3c. An average attribute data-vector is extracted around well A (Figure 3a and b) from this zone. We call this as shale petrotype A. Petrotype A (well data vector) shows a higher lambda-rho value compared to the mu-rho and the P-impedance (Figure 3b).

Zone B is defined within the upper section of the Lower Barnett Shale. An average attribute data-vector (Shale petrotype B) is extracted around well B (Figure 3a and b) from this zone. This zone mostly has siliceous non-calcareous shale lithofacies (Singh, 2008). Petrotype B shows a low lambda-rho and P-impedance (Figure 3b).

Zone C is defined within the lower section of the Lower Barnett Shale. The shale petrotype C is extracted around well C (Figure 3a and b) from this zone. This lowermost Barnett Shale is the zone of hot shale (Pollastro et al., 2007) with very high gamma ray. Petrotype C shows a low lambda-rho and P-impedance.

We use the three distance measures (explained before) to classify the attribute data vectors based on these shale petrotypes A, B and C (target vectors) in the Barnett shale formation.

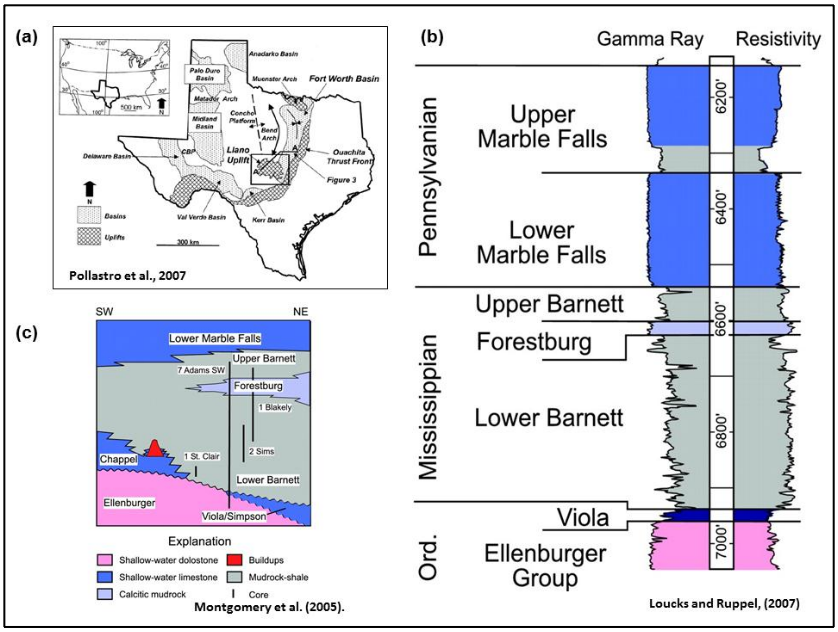

Figure 2: (a) The map of Texas highlighting major basins and uplifts. This Ft. Worth basin is bounded by the Muenster Arch to the northeast, the Ouachita Thrust Front to the east, the Bend Arch to the west, the Red River Arch to the north, and the Llano Uplift to the south. (b) Stratigraphic section including the Gamma ray and the resistivity log showing the major units. The Barnett sits on an angular unconformity above the Cambrian to upper-Ordovician-age carbonates of the Ellenberger Group and Viola Formation and overlying Pennsylvanian-age Marble Falls Limestone with the Forestburg Limestone in dividing the Barnett formation. (c) Cross-section of the stratigraphy of Ft. Worth basin from Montgomery et al. (2005).

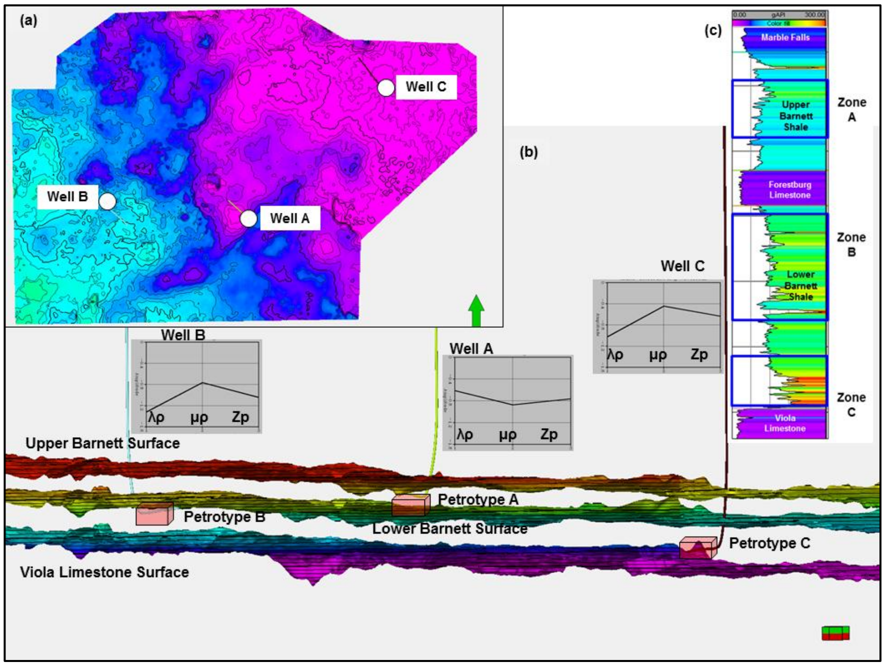

Figure 3: (a) The Location of the three horizontal wells Well A, Well B and Well C overlaid over the upper Barnett time horizon of the 3D survey. (b) The location of the wells and their horizontal extension within the Barnett zone and the sub-volumes for extracting an average well-data vector. (c) The zones for extracting the average well data-vector are highlighted on a gamma ray log from the survey. Shale petrotype-A is extracted from a zone within the upper Barnett shale, shale petrotype-B facies is extracted from the upper region of the lower Barnett zone, and petrotype-C is extracted from the "hot" gamma ray region of the lower Barnett shale.

Discussion

Each of the three zones A, B and C within the Barnett shale formation are analyzed separately and separate algorithm outputs separate classification volumes, which will be discussed subsequently. Each zone has five separate volumes; one from minimum Euclidean distance measure (MED), one from spectral angle mapper (SAM) and three PDF similarity volumes from GTM classification (Figures 4, 5, and 6). The results from each of the classification volumes are analyzed and a comparative study is made.

Figure 4 shows the comparative study of all the five volumes from the Upper Barnett shale (zone A). The average well data-vector is extracted around Well A, which acts as the target vector. The MED classification (Figure 4b) and the SAM classification (Figure 4c) give similar results around the well (cyan color facies). However, the shale petrotype-A spatially varies over the survey depending on the cutoff factor between MED and SAM. The PDF similarity measure from Bhattacharya measure has three separate volumes (Figure 4d, 4e and 4f) corresponding to the three predefined shale petrotypes. Analysis shows that the Upper Barnett zone has mostly rocks belonging to petrotype-A (Figure 4d). However some rocks in this zone A have properties similar to petrotype C (Figure 4f). Further we infer that it is extremely unlikely that the petrotype-B is present in this zone (Figure 4e).

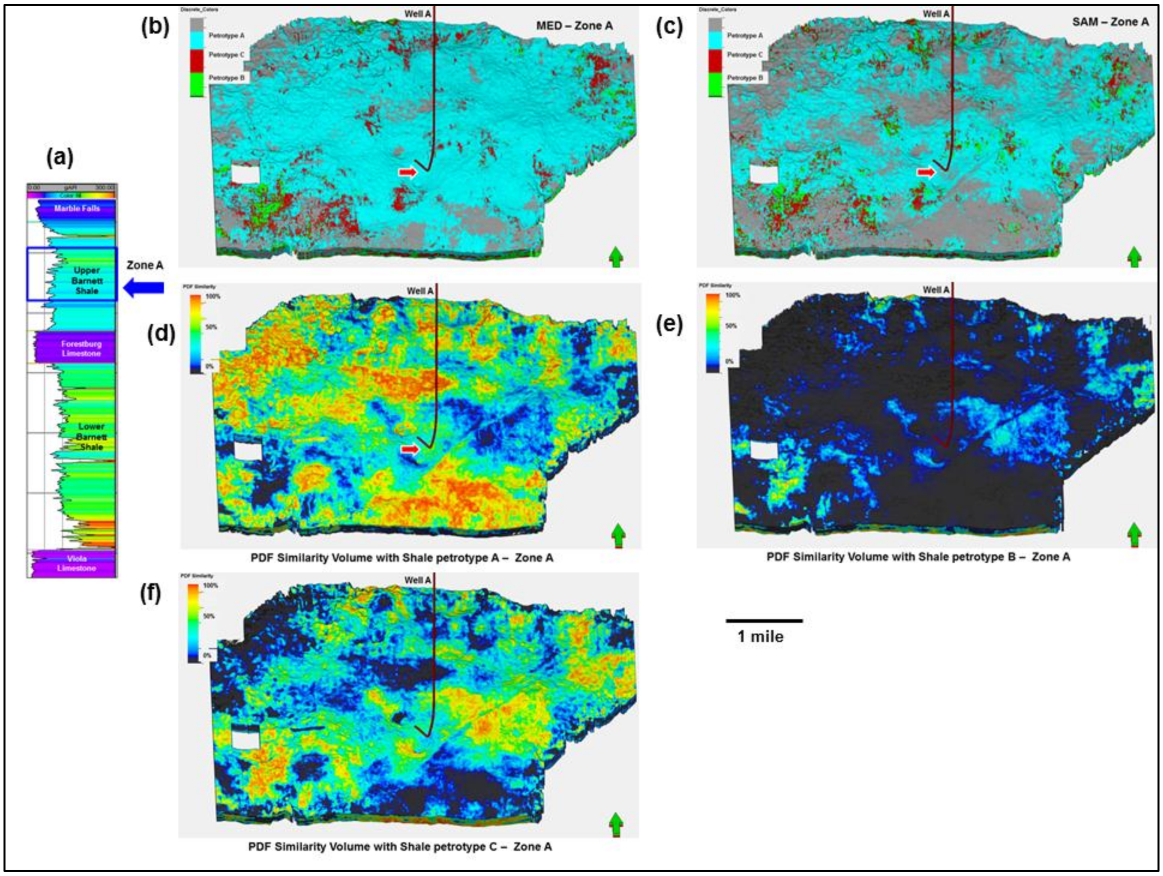

Figure 4: Supervised classification analysis for Zone A, which corresponds to the Upper Barnett zone. (a) The shale facies petrotype-A is extracted from this upper Barnett shale (blue arrow) around the Well A (red arrow). The shale petrotype A is colored cyan, shale petrotype B is colored green and the shale petrotype C is colored red. Strata slice within zone A from the results of (b) Minimum Euclidean Distance (MED) measure and (c) Spectral Angle mapper (SAM). The regions similar to shale petrotype-A (from the MED classification and the SAM classifier) are colored cyan. The gray areas in b and c are unclassified and do not belong to any of the pre-defined shale petrotype. Figure c, d, and e show the results of supervised GTM analysis. The "red" color in the colorbar highlights regions with highest probability and the "dark grey" corresponds to the least probability, respectively of occurrence of the petrotype-A shale facies. (c) PDF Similarity volume for the petrotype -A facies. The stratal slice shows that petrotype-A is abundant in this zone. (d) PDF Similarity volume showing the probability of occurrence of shale petrotype-B (corresponding to zone B) within zone A. Mostly dark gray color highlights that the petrotype B has the least probability of occurrence in zone A. (e) The probability of occurrence of the petrotype-C (corresponding to the hot-gamma zone C) are color-coded on the strata-slice. The analysis shows that there are localized occurrences of the petrotype-C in zone A.

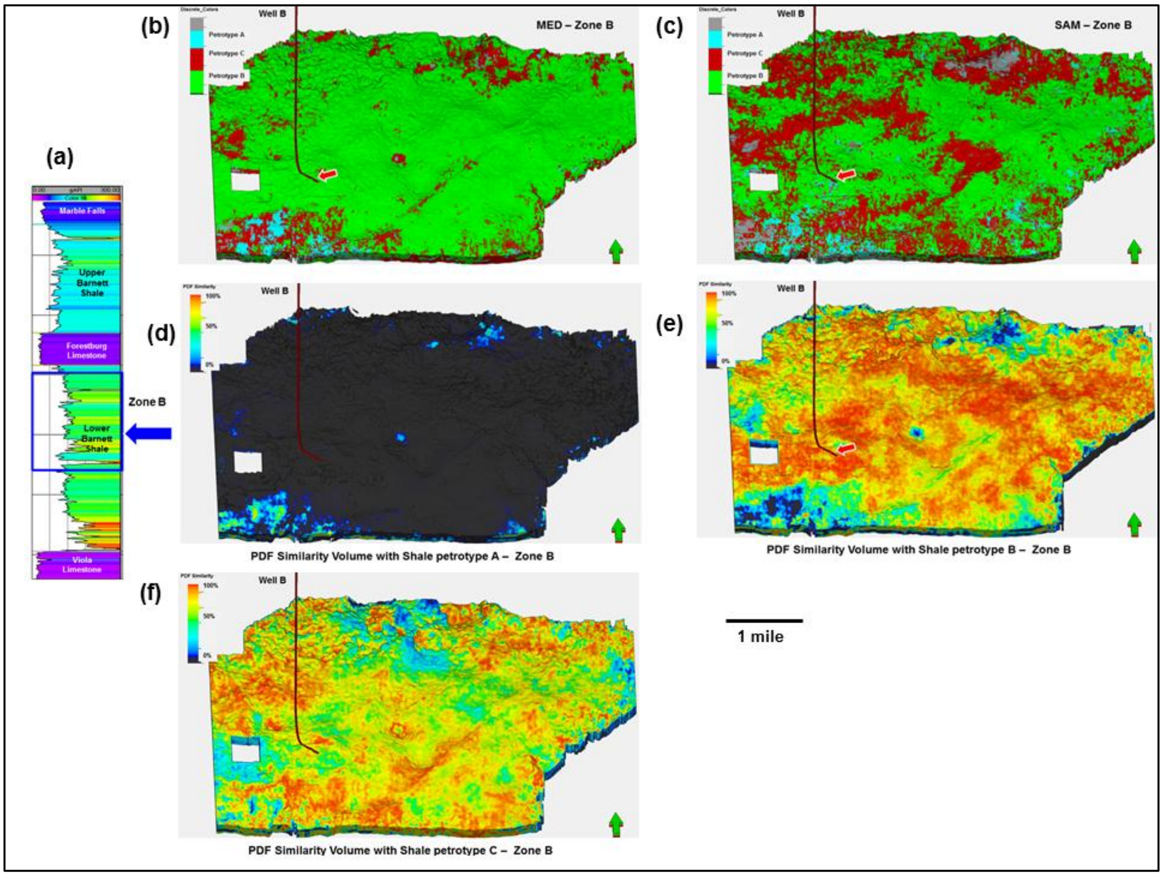

Figure 5: Supervised classification analysis for Zone B, which corresponds to the upper region of Lower Barnett zone. (a) The shale petrotype-B is extracted from this upper region of Lower Barnett zone (blue arrow) around the Well B (red arrow). The shale facies A is colored cyan, shale petrotype B is colored green and the petrotype C is cored red. Strata slice within zone B from the results of (b) Minimum Euclidean Distance (MED) measure and (c) Spectral Angle mapper (SAM). The regions similar to shale petrotype-B (from the SAM classification and the MED classifier) are colored green. Regions similar to Type-C shale facies are colored red. Figure c, d, and e show the results of supervised GTM analysis. The "red" color in the colorbar highlights regions with highest probability and the "dark grey" corresponds to the least probability of occurrence respectively of the Type-B shale facies. (c) PDF Similarity volume for the Type-A facies. Mostly dark gray color highlights that the shale petrotype A has the least probability of occurrence in zone B. (d) PDF Similarity volume showing the probability of occurrence of shale petrotype-B (corresponding to zone B) within zone B. Zone B shows the highest probability of spatial occurrence of Type B shale facies. (e) The probability of occurrence of the petrotype-C (corresponding to the hot-gamma zone C) are color-coded on the strata-slice. The analysis shows that there are localized occurrences of the petrotype-C in zone B.

Figure 5 above shows the comparative study of all the five volumes from the upper region of Lower Barnett shale (zone B). The average well data-vector is extracted around Well B, which acts as the target vector. The MED classification (Figure 5b) and the SAM classification (Figure 5c) give similar results around the well (green color facies). However, the shale petrotype-B spatially varies over the survey for SAM classifier compared to MED classifier, which is varying less spatially. We see the presence of petrotype C (red color facies) in this zone from the SAM classifier. The PDF similarity measure from Bhattacharya measure has three separate volumes (Figure 5d, 5e and 5f) corresponding to the three predefined shale petrotypes. Analysis shows that the upper region of Lower Barnett zone has mostly rocks belonging to petrotype-B (Figure 5e) and less of petrotype-C (Figure 5f). We infer that it is extremely unlikely that the petrotype-A is present in this zone (Figure 5d). Generally this region of the Lower Barnett shale has siliceous non-calcareous shale lithofacies (Singh, 2008) and is brittle in nature (Perez, 2013). Shale petrotype B corresponds to brittle shale. Mapping these brittle zones is helpful because these are the regions where a horizontal well can be placed for effective fracturing.

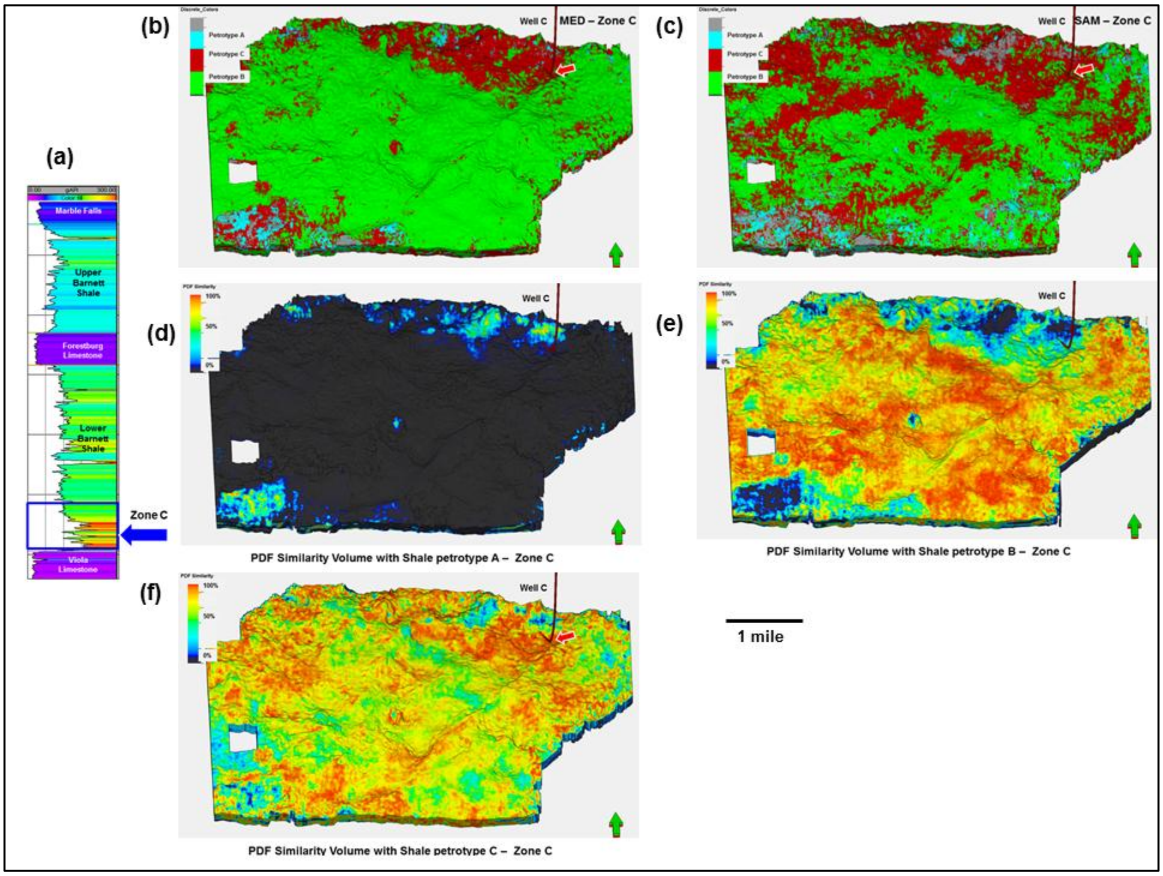

Figure 6: Supervised classification analysis for Zone C, which corresponds to the lower region of Lower Barnett zone. (a) The shale petrotype-C is extracted from this lower region of Lower Barnett zone (blue arrow) around the Well C (red arrow). The shale facies A is colored cyan, shale petrotype B is colored green and the petrotype C is cored red. Strata slice within zone C from the results of (b) Minimum Euclidean Distance (MED) measure and (c) Spectral Angle mapper (SAM). The regions similar to shale petrotype-B (from the SAM classification and the MED classifier) are colored green. Regions similar to Type-C shale facies are colored red. Figure c, d, and e show the results of supervised GTM analysis. The "red" color in the colorbar highlights regions with highest probability and the "dark grey" corresponds to the least probability of occurrence respectively of the Type-B shale facies. (c) PDF Similarity volume for the Type-A facies. Mostly dark gray color highlights that the shale petrotype A has the least probability of occurrence in zone B. (d) PDF Similarity volume showing the probability of occurrence of shale petrotype-B (corresponding to zone B) within zone B. Zone B shows the highest probability of spatial occurrence of Type B shale facies. (e) The probability of occurrence of the petrotype-C (corresponding to the hot-gamma zone C) are color-coded on the strata-slice. The analysis shows that there are localized occurrences of the petrotype-C in zone B.

Figure 6 above shows the comparative study of all the five volumes from the lower region of Lower Barnett shale (zone C). The average well data-vector is extracted around Well C, which acts as the target vector. The MED classification (Figure 6b) and the SAM classification (Figure 6c) give similar results around the well (red color facies). However, the shale petrotype-C spatially varies over the survey for SAM classifier compared to MED classifier, which is varying less spatially. We see the presence of petrotype B (green color facies) in this zone from the SAM classifier. The three separate volumes from PDF similarity measure (Figure 6d, 6e and 6f) correspond to the three predefined shale petrotypes. Analysis show that within the survey this zone C has mostly rocks belonging to petrotype-B (Figure 6e) and petrotype-C (Figure 6f). We infer that it is extremely unlikely that the petrotype-A is present in this zone (Figure 6d). From the study it is evident that the northeast corner of the survey around the well C, it is mainly shale petrotype C. Petrotype B is present mostly in the center and south of the survey. The SAM results are more consistent with the PDF similarity outputs. Shale petrotype C corresponds to the high gamma values in the well logs and corresponds to regions of most ductile shale, which may be due to high TOC concentration in this zone (Singh, 2008 and Perez, 2013).

Conclusions

In the paper, we have studied the three different supervised distance metric classifiers when applied on the multi-attribute seismic data from the Barnett shale in the Fort Worth Basin. Our results demonstrate the unique divergence properties of the three distance metrics discussed in the paper when seen on facies classification outputs. In all the three zones of our case study, it is evident that the SAM classifier results are more consistent with the PDF similarity results. The mapped brittle zones and the mapped high TOC zones are consistent within the results of the SAM classifier and the PDF similarity. In this study we have tried to demonstrate that the classification based on distance metrics have significant value in the identification and classification heterogeneous Barnett shale.

Acknowledgements

We thank Devon Energy for use their seismic and well data over the Barnett Shale in this work. Financial support for this effort was provided by the industry sponsors of the Attribute-Assisted Seismic Processing and Interpretation (AASPI) consortium. All the 3D seismic displays were made using licenses to Petrel, provide to OU for research and education courtesy of Schlumberger.

References

Bishop, C. M., M. Svensen, and C. K. I. Williams, 1998, The generative topographic mapping: Neural Computation, 10, No. 1, 215-234.

Duda, R.O., Hart, P.E, Stork, D.E., *Pattern Classification*, 2nd Edition, Wiley, 2000, ISBN 978-0-471-05669-0.

Boardman, 1992, SIPS User's Guide Spectral Image Processing System, Version 1.2, Center for the Study of Earth from Space, Boulder, CO. 88 pp.

Michelena, J. R., E. S. M. Gonzalez, and M. Capello, 1998, Similarity analysis: A new tool to summarize seismic attribute information: The Leading Edge, **17**, 1361-1364

Montgomery, S. L., D. M. Jarvie, A. K. Bowker, and M. R. Pollastro, 2005, Mississippian Barnett Shale, Fort Worth Basin, north central Texas: Gas-shale play with multi-trillion cubic foot potential, AAPG Bulletin; February 2005; **89**; 155-175.

Perez-Altamar, R., 2013, Correlation of surface seismic measurements to completion quality: Application to the Barnett Shale, PhD dissertation, the University of Oklahoma.

Pollastro, R. M., D. M. Jarvie., R. J. Hill, and C. W. Adams, 2007, Geologic framework of the Mississippian Barnett Shale, Barnett-Paleozoic total petroleum system, Bend Arch-Fort Worth Basin, Texas: AAPG Bulletin, **91**, 405-436.

Poupon, M., Gil, J., D. Vannaxay, and B. Cortiula, Tracking Tertiary delta sands (Urdaneta West, Lake Maracaibo, Venezuela): An integrated seismic facies classification workflow, The Leading Edge, **23**, 909-912.

Singh, P., 2008, Lithofacies and Sequence Stratigraphic Framework of the Barnett Shale, Northeast Texas: Ph.D. dissertation, University of Oklahoma.

Roy, A., 2013, Latent space classification of seismic facies: PhD dissertation, the University of Oklahoma.

Roy, A., Jayaram, V., Marfurt, K.J., 2013, Active learning algorithms for 3D seismic facies classification, extended abstract SEG Annual Meeting, Sept. 2013, Houston, TX, USA.